Bioluminescence Tomography by an Iterative Reweighted l_2-Norm Optimization

Ping Wu, Yifang Hu, Kun Wang, and Jie Tian*, *Fellow, IEEE*

***Abstract*—Bioluminescence tomography is a promising tool in preclinical research, enabling noninvasive real-time *in vivo* imaging as well as quantitative analysis in small animal studies. Due to the difficulty of reconstruction, continuous efforts are still made to find more practical and efficient approaches. In this paper, we present an iterative reweighted l_2-norm optimization incorporating anatomical structures in order to enhance the performance of bioluminescence tomography. The structure priors have been utilized to generate a heterogeneous mouse model by extracting the internal organs and tissues, which can assist in establishing a more precise photon diffusion model, as well as reflecting a more specific position of the reconstruction results inside the mouse. To evaluate the performance of the iterative reweighted approach, several numerical simulation studies including comparative analyses and multisource cases have been conducted to reconstruct the same datasets. The results suggest that the proposed method is able to ensure the accuracy, robustness, and efficiency of bioluminescence tomography. Finally, an *in vivo* experiment was performed to further validate its feasibility in a practical application.**

***Index Terms*—Bioluminescence tomography, hybrid imaging, optical molecular imaging (OMI), 3-D reconstruction.**

I. Introduction

OPTICAL molecular imaging (OMI) has played an increasingly important role in revealing the dynamic interactions of cellular processes at different system levels [1]–[4]. Bioluminescence imaging is one of the various modalities of OMI, which has attracted considerable attention because of its high sensitivity and low cost. It utilizes an ultrasensitive CCD camera to detect light emitted by living cells expressing a luciferase gene, allowing researchers to monitor the cell growth and to localize tumors in small animals [5]–[8]. Recently, bioluminescence tomography has become possible. It has upgraded the 2-D bioluminescence imaging to 3-D *in vivo* detection, providing convenience for researchers in more accurate localization of internal bioluminescent sources and quantitative analysis of the bioluminescent density.

This newly developed technology has facilitated preclinical applications in biomedical *in vivo* studies, such as tumor detection at an early stage, stem cell imaging, and drug efficacy evaluation [9]–[12]. Compared with some other imaging modalities, bioluminescence tomography has a higher sensitivity capable of reflecting biological changes at the cellular level. It costs much less to build a bioluminescence tomography system than to set up a PET or an MRI system in terms of the instrumentation. Besides, the expenditures on experimental animals are partly saved because bioluminescence tomography enables noninvasive imaging; thus, fewer animals are needed for one trial. Moreover, bioluminescence tomography can realize 3-D visualization in real time, while animals are usually required to be sacrificed after the experiment for further observation in the conventional way.

One of the challenging problems in bioluminescence tomography is that multiple scattering of photons propagating through heterogeneous biological tissues makes it a highly ill-posed inverse problem. Besides, the only known information available for the 3-D reconstruction is the photon distribution on the boundary of the target, which leads to a mathematical process of solving an underdetermined system of linear equations. Wang *et al.* first theoretically proved that the bioluminescent sources can be uniquely and accurately recovered by incorporating sufficient *a priori* information to alleviate the ill-posedness [13]. As reported in the existing literature, multiple types of *a priori* information have been adopted in reconstruction algorithms of bioluminescence tomography ranging from the permissible source region and spectral information to more involved sparse constraint [14]–[20]. The basic idea is to reduce the number of unknown variables or to increase the amount of known boundary measurements.

The other difficulty is that the numerical computation of reconstruction could be time consuming and inefficient due to the large scale of datasets. A variety of reconstruction algorithms have been proposed, such as the Guass–Newton method, conjugate gradient method (CG), interior-point method, etc. [21]–[24]. Recently, bioluminescent signals were found to have a similar property of sparse signals, i.e., there were zeros everywhere except on the minimal support of solution space. Consequently, the approaches of sparse signal recovery have become

Manuscript received April 23, 2013; revised July 19, 2013; accepted August 13, 2013. Date of publication August 21, 2013; date of current version December 16, 2013. This work was supported in part by the National Basic Research Program of China (973 Program) under Grant 2011CB707700, in part by the Knowledge Innovation Project of the Chinese Academy of Sciences under Grant KGCX2-YW-907, in part by the National Natural Science Foundation of China under Grants 81227901, 61231004, 81027002, and 81261120414, in part by the Chinese Academy of Sciences Visiting Professorship for Senior International Scientists under Grant 2012T1G0036, and in part by the Beijing Natural Science Foundation under Grant 4111004. *Asterisk indicates corresponding author.*

P. Wu and K. Wang are with the Key Laboratory of Molecular Imaging and Functional Imaging, Institute of Automation, Chinese Academy of Sciences, Beijing 100190, China (e-mail: ping.wu@ia.ac.cn; kun.wang@ia.ac.cn).

Y. Hu is with the Department of Biomedical Engineering, School of Computer and Information Technology, Beijing Jiaotong University, Beijing 100044, China (e-mail: huyifang@fingerpass.net.cn).

*J. Tian is with the Key Laboratory of Molecular Imaging and Functional Imaging, Institute of Automation, Chinese Academy of Sciences, Beijing 100190, China (e-mail: tian@ieee.org).

Color versions of one or more of the figures in this paper are available online at http://ieeexplore.ieee.org.

Digital Object Identifier 10.1109/TBME.2013.2279190

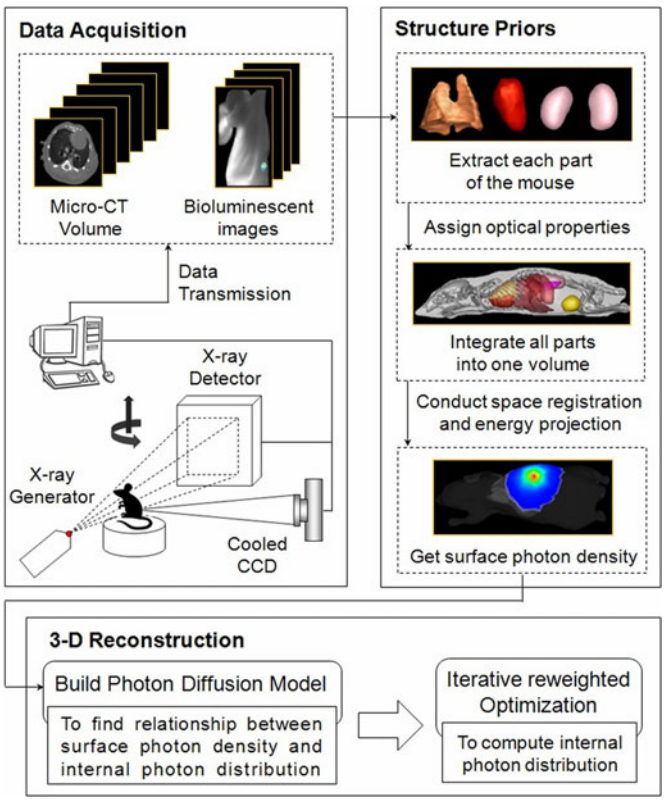

Fig. 1. Method overview.

increasingly popular in bioluminescence tomography, surpassing the classical optimization techniques in reconstruction efficiency. The essence of sparse signal recovery is to utilize limited linear observations via the norm optimal strategy. A number of iterative algorithms which have been studied to recover sparse signals include the Born iterative method, truncate-Newton, Levenberg–Marquardt approach, etc. [25]–[27].

Although there are many challenging problems in bioluminescence tomography, consistent efforts are still being made to develop more advanced reconstruction methods combined with *a priori* knowledge for a more practical application. In this paper, we demonstrate an efficient algorithm using an iterative reweighted l_2-norm optimization, while taking the structural information as priors to localize the bioluminescent signals. Furthermore, both the numerical simulation studies and *in vivo* mouse studies have been carried out to evaluate the feasibility and limitations of the proposed method. Finally, their results have been compared with those of the classical reconstruction algorithms, and the multisource cases have also been designed to test the performance of the proposed method.

II. Materials and Methods

There are mainly three steps to implement the proposed algorithm using the iterative reweighted l_2-norm optimization with structure priors for bioluminescence tomography. The whole process is depicted by Fig. 1. First, the datasets including micro-CT volume and bioluminescence images were obtained by the experimental system. Then, the structure priors provided by

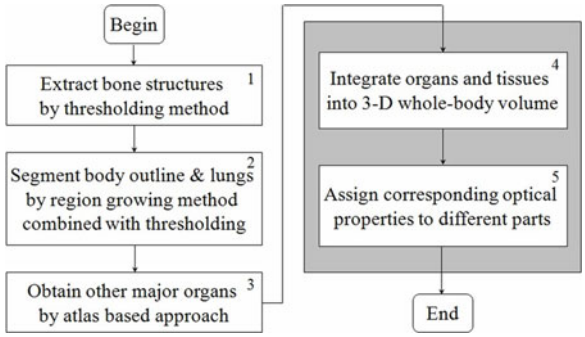

Fig. 2. Procedure of building the heterogeneous mouse model.

micro-CT were employed to generate a heterogeneous mouse model by extracting the internal organs and tissues from the experimental mouse, which can assist in establishing a more accurate photon diffusion model for bioluminescence tomography. Third, an optimization function based on this forward model was built for subsequent optimization. By introducing a weight function into the optimization function, the original l_p-norm problem was converted to a more simple form of the l_2 norm. Afterward, an iterative shrinkage operator was utilized to avoid the operation of matrix inversion, which can reduce the computational complexity.

A. Experimental System and Data Acquisition

During imaging, the optical/micro-CT imaging system developed by our group [28], [29] was used to acquire the experimental datasets, which is an integrative platform that combines bioluminescence and fluorescence imaging with an X-Ray CT scanning. Here, two modalities including bioluminescence imaging and X-Ray CT were applied to perform the mouse experiment. For micro-CT scanning, the cone-beam X-ray generator was operated in a continuous mode with the tube voltage being 55 kVp, where 360° projections were scanned. For bioluminescence imaging, an ultrasensitive cooled CCD camera with a 13 μm $\times$ 13 μm pixel size was involved in taking the multiview optical images. In the *in vivo* experiment, a hairless mouse was injected with Fenestra LC and anesthetic. Then, a home-made luminescent bead with a plastic wrap was implanted into the mouse liver.

B. Structure Priors of the Heterogeneous Mouse Model

As it is known, bioluminescence tomography is a typical ill-posed inverse problem with a large number of unknowns and a relatively limited number of boundary measurements. It is indispensable in incorporating *a priori* information into the inverse problem formulation in order to obtain viable solutions. Besides employing the sparse constraint in Section II-D, we also utilized the anatomical structure information acquired by micro-CT here. The structure priors can aid in generating a heterogeneous mouse model by a hybrid segmentation approach briefly illustrated in Fig. 2.

The heterogeneous model describes the anatomical structure of the experimental mouse in three dimensions, containing the

major organs and tissues, as well as their corresponding optical absorption coefficient and optical diffusion coefficient. The overall procedure consists of five steps as follows.

1) For the tissues and organs which show higher contrast on CT images, such as the skeleton, stomach, and bladder, they were automatically extracted by a thresholding method.
2) For the parts which have lower contrast on CT but occupy a relatively larger area such as the body outline and lungs, these were segmented by a region growing method combined with thresholding.
3) Regarding other major organs such as the heart, liver, and kidneys, they were extracted by an atlas-based approach. It firstly built an average-shaped atlas, then roughly localized the organs, and finally made precise registration.
4) After obtaining the above separate volumes, we needed to integrate them into one volume data, where the priorities have been set for different organs and tissues to eliminate the inevitable overlaps and holes.
5) The corresponding optical properties of different parts were assigned to depict the interaction of the internal bioluminescent signals with different biological tissues. The optical properties in this paper were mainly composed of the absorption coefficient and the scattering coefficient, which were measured by diffusion optical tomography.

Finally, a heterogeneous anatomical mouse model was completed, offering sufficient *a priori* knowledge to guide the following process of building a more accurate photon diffusion model for 3-D reconstruction, as well as reflecting a more specific position of the reconstruction results inside the mouse.

C. Photon Diffusion Model

To describe how the photons transport through biological tissues, the diffusion equation was adopted to model light propagation [30], which is defined as

$$-\nabla \cdot \left[D\left(\mathbf{r}\right)\nabla\Phi\left(\mathbf{r}\right)\right] + \mu_a\left(\mathbf{r}\right)\Phi\left(\mathbf{r}\right) = S\left(\mathbf{r}\right) \quad \mathbf{r} \in \Omega \tag{1}$$

where D is the optical diffusion coefficient, $\mathbf{r}$ is the position vector, Φ is the photon flux density, μ_a is the absorption coefficient, S is the internal source distribution, and Ω is the region of the biological tissues. D is calculated by

$$D = \frac{1}{3\left[\mu_a + (1-g)\,\mu_s\right]} \tag{2}$$

where μ_s is the scattering coefficient and g is the anisotropy parameter. The diffusion equation is accompanied by the Robin boundary condition, which is given by

$$\Phi\left(\mathbf{r}\right) + 2\kappa\left(n\right)D\left(\mathbf{r}\right)\left[v\left(\mathbf{r}\right)\cdot\nabla\Phi\left(\mathbf{r}\right)\right] = 0 \quad \mathbf{r} \in \partial\Omega \tag{3}$$

where $\boldsymbol{\kappa}$ is the boundary mismatch factor between the biological tissues and air, n is the refractive index of the biological tissues, v is the unit outward normal on $\partial\Omega$, and $\partial\Omega$ is the boundary of the biological tissues. $\boldsymbol{\kappa}$ is calculated by

$$\kappa\left(n\right) = \frac{1 + \left(1.4399n^{-2} + 0.7099n^{-1} + 0.6681 + 0.636n\right)}{1 - \left(1.4399n^{-2} + 0.7099n^{-1} + 0.6681 + 0.636n\right)}. \tag{4}$$

The theoretical outgoing photon distribution on the boundary of the biological tissues is

$$\Gamma\left(\mathbf{r}\right) = -D\left(\mathbf{r}\right)\left[v\left(\mathbf{r}\right)\cdot\nabla\Phi\left(\mathbf{r}\right)\right] = \frac{\Phi\left(\mathbf{r}\right)}{2\kappa(n)} \quad \mathbf{r} \in \partial\Omega\,. \tag{5}$$

After applying the process of discretization by finite element formulation to the photon diffusion model, we established the linear relationship between the measured outgoing photon distribution on the surface and the unknown internal photon distribution via replacing the variables with the matrix-vector forms

$$\mathbf{MS} = \mathbf{\Gamma} \tag{6}$$

where $\mathbf{M}$ is the system matrix standing for the optical properties of the heterogeneous mouse model and Γ is the surface photon distribution acquired by the ultrasensitive CCD camera of the experimental system. Therefore, the ultimate aim of bioluminescence tomography is to recover the bioluminescent source distribution $\mathbf{S}$ in the above linear equation by an effective optimization strategy.

D. Iterative Reweighted l_2-Norm Optimization

The approaches of sparse signal recovery have recently become appealing alternatives to reconstruct the internal photon distribution because the bioluminescent signals have a similar property of sparse signals. Those algorithms basically depend on the norm optimal strategy to recover the limited linear observations in a computationally effective way, where the required number of samples could be less than the quantity needed by the Nyquist sampling theorem. For this reason, the newly emerged methods of sparse signal recovery are appropriate for solving the underdetermined system of linear equations in bioluminescence tomography.

To find the best basis that stands for the bioluminescent signals, one of the effective algorithms will be introduced in this section, which is named the iterative reweighted l_2-norm optimization [31], [32]. This approach is then mathematically derived as follows.

1) To Begin With the Original Optimization Function: The ultimate aim of using the iterative reweighted optimization is to achieve the unknown internal photon distribution $\mathbf{S}$ in Eq. (6), while the classical solution to Eq. (6) can be generally expressed in the following form [33]:

$$\arg\min_{s}\left[\frac{1}{2}\left\|\mathbf{MS}-\mathbf{\Gamma}\right\|_2^2 + \lambda\left\|\mathbf{S}\right\|_p^p\right] \tag{7}$$

where λ is the regularization parameter, $\|\cdot\|_2^2$ represents the l_2 norm, $\|\cdot\|_p^p$ stands for the l_p norm, and p is a real number in the range from 1 to 2.

2) To Simplify the Optimization Function by Introducing a Weight Function: The last term in Eq. (7) involves the l_p norm, which is usually more complex than the l_2 norm during computation. To convert the l_p-norm problem into the l_2-norm form, the term $\|\mathbf{S}\|_p^p$ is substituted with $\mathbf{S}^{\mathrm{T}}\mathbf{W}^{-1}(\mathbf{S})\mathbf{S}$. As defined in Eq. (8), $\mathbf{W(S)}$ is a weight function, which is a diagonal matrix with the values $|\mathbf{S}[\mathrm{k}]|^{2-p}$ in its main diagonal. Here, k is an

integer greater than or equal to zero, and $\mathbf{S}[k]$ means the kth element in $\mathbf{S}$:

$$\mathbf{W}(\mathbf{S}) = \begin{bmatrix} |\mathbf{S}[0]|^{2-p} & & & \\ & |\mathbf{S}[1]|^{2-p} & & \\ & & \ddots & \\ & & & |\mathbf{S}[k]|^{2-p} \end{bmatrix}. \quad (8)$$

Then, Eq. (6) can be rewritten in the l_2-norm form with the weight function as Eq. (9), which has become easier to optimize because p does not exist anymore:

$$\arg\min_{S} \left[\frac{1}{2} \|\mathbf{MS} - \Gamma\|_2^2 + \lambda \mathbf{S}^{\mathrm{T}} \mathbf{W}^{-1}(\mathbf{S}) \mathbf{S} \right]. \quad (9)$$

3) To Accelerate the Computation by Employing an Iterative Shrinkage Operator: The computation of the optimal values will be slow if we have to calculate the inversion of **W(S)** in Eq. (9), so an iterative shrinkage operator **P** is employed as Eq. (10). It can help to avoid the operation of matrix inversion which usually takes up lots of system memory and time:

$$\mathbf{P} = \left(\frac{2\lambda}{\alpha} \mathbf{I} + \mathbf{W}(\mathbf{S}_j) \right)^{-1} \mathbf{W}(\mathbf{S}_j). \quad (10)$$

In the above equation, $\mathbf{I}$ is a unit matrix, α represents a relaxation constant and it is not less than 1, and j is an integer greater than or equal to zero.

4) To Find the Optimal Values by Using an Iterative Method: With the help of the iterative shrinkage operator **P**, we can finally solve the optimization function by means of iteration. The iterative equation is given in Eq. (11), which stands for the relationship between $\mathbf{S}_{j+1}$ and $\mathbf{S}_j$. Here, $\mathbf{S}_j$ represents the jth estimate of the internal source distribution, and the initial value $\mathbf{S}_0 = 0.001$ when $j = 0$. The iterative optimization will stop when the ratio $R = \mathbf{S}_{j+1} / \mathbf{S}_j \leq 0.1$ is satisfied:

$$\mathbf{S}_{j+1} = \mathbf{P} \left(\frac{1}{\alpha} \mathbf{M}^T (\mathbf{\Gamma} - \mathbf{MS}_j) + \mathbf{S}_j \right). \quad (11)$$

The procedure of reconstructing the bioluminescent source distribution **S** inside the biological tissues by the proposed method has been concisely summarized in Fig. 3.

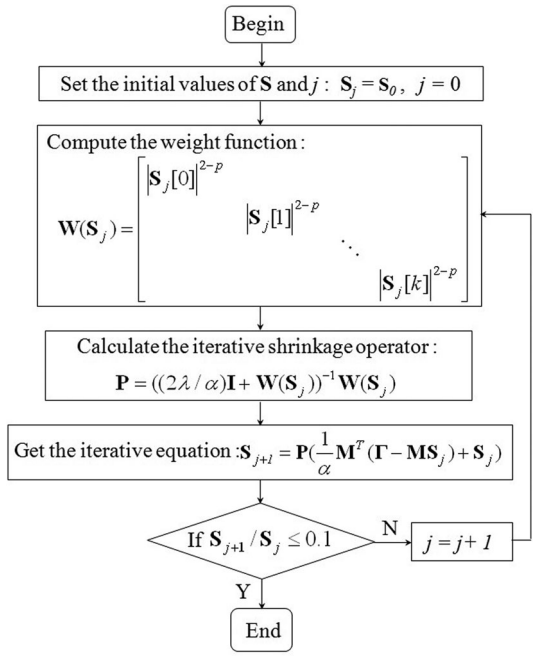

Fig. 3. Procedure of iterative reweighted l_2-norm optimization.

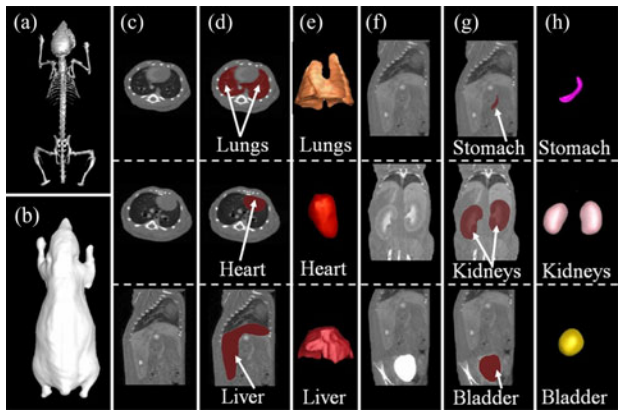

Fig. 4. Segmentation results: (a) skeleton; (b) body outline; (c), (f) 2-D slices of the X-Ray CT data; (d), (g) 2-D slices of the X-Ray CT data with segmentation regions marked; (e), (h) organs rendered in 3-D.

III. Results and Discussion

In this section, both numerical simulation studies and *in vivo* mouse studies have been designed to analyze the accuracy, robustness, and efficiency of the proposed method. All of the computational processing was completed on a personal computer with 3.20 GHz Intel Core i5 CPU and 3 GB RAM.

A. Results of the Heterogeneous Mouse Model

To generate the heterogeneous mouse model, the original dataset acquired by micro-CT was converted into 3-D volume data using the classical Feldkamp–Davis–Kress algorithm. Then, the volume data were processed by the hybrid segmentation method and the major parts of the experimental mouse were extracted in sequence. The segmentation results are visualized in Fig. 4, where Fig. 4(a) shows the 3-D skeleton, while Fig. 4(b) renders the surface of the mouse body. Other organs and tissues are visualized in both 2-D and 3-D from Fig. 4(c) to (h). Take the first row of Fig. 4(c)–(e) as an example. Fig. 4(c) is one of the raw CT slices in 2-D, followed by marking the region of the lungs on the same slice in a darker color which represents the current segmentation area shown in Fig. 4(d). After the lungs were successfully extracted, they were finally displayed in 3-D as depicted in Fig. 4(e).

Comparing Fig. 4(c) and (f), and Fig. 4(d) and (g), we can visually assess the segmentation quality. The results suggest that the hybrid segmentation method enables extraction of some major organs and tissues from the experimental mouse. By integrating all of the separate parts, we ultimately obtained the whole-body anatomical structure of the mouse as shown in Fig. 5. Therefore, a heterogeneous mouse model for reconstruction was established, where the corresponding optical properties were

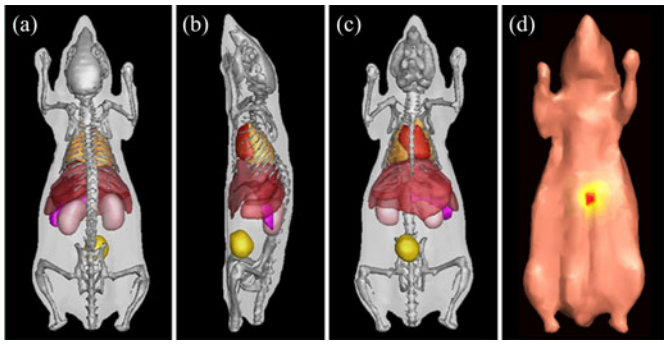

Fig. 5. Heterogeneous mouse model: (a) front view; (b) side view; (c) rear view; (d) with photon distribution of the bioluminescent signals on the surface.

TABLE I
OPTICAL PROPERTIES OF MOUSE ORGANS AND TISSUES

	Numerical Simulation Study		*In vivo* Mouse Study	
	μ_a (mm^{-1})	D(mm^{-1})	μ_a (mm^{-1})	D(mm^{-1})
Lungs	1.4e-3	0.1571	7.1e-3	0.1445
Heart	5.8e-4	0.3661	2.2e-3	0.2944
Liver	2.0e-3	0.5112	1.2e-2	0.4318
Muscle	6.9e-4	0.8756	3.2e-3	0.5619
Stomach	5.7e-4	0.2414	-	-
Kidneys	8.0e-4	0.1579	-	-
Bone	3.6e-4	0.1424	2.2e-3	0.1137

assigned to different organs and tissues according to Table I. Then, the Molecular Optical Simulation Environment (MOSE) (http://www.mosetm.net/) was applied to simulate the surface photon distribution emitted by the bioluminescent signals inside the heterogeneous mouse model for numerical simulation studies, as depicted in Fig. 5(d).

B. Reconstruction Results: One-Source Case

1) Accuracy: The reconstruction results for the one-source case in the numerical simulation studies are given in Fig. 6. A simulated bioluminescent source was set by MOSE, whose center coordinate was (20.00, 12.00, 55.00) and the power source was 1.6 nW/mm^3. After reconstruction by the iterative reweighted l_2-norm optimization, the result based on a heterogeneous mouse model in 3-D view is shown in Fig. 6(a) when $\lambda = 10^{-3}$. Its cross-sectional view is displayed in Fig. 6(e), where the reconstruction center coordinate was (20.63, 12.35, 55.25), resulting in a reconstruction error of 0.76 mm. As depicted in Fig. 6(d), the reconstruction error sharply increased to 1.84 mm when the reconstruction was based on a homogeneous mouse model without any anatomical information. This is mainly because the heterogeneous model considers the specific optical properties of the organs and tissues leading to a more accurate description of photon propagation.

To compare the reconstruction accuracy, two other classical algorithms have been utilized to reconstruct the same datasets while maintaining the same termination condition. One was the

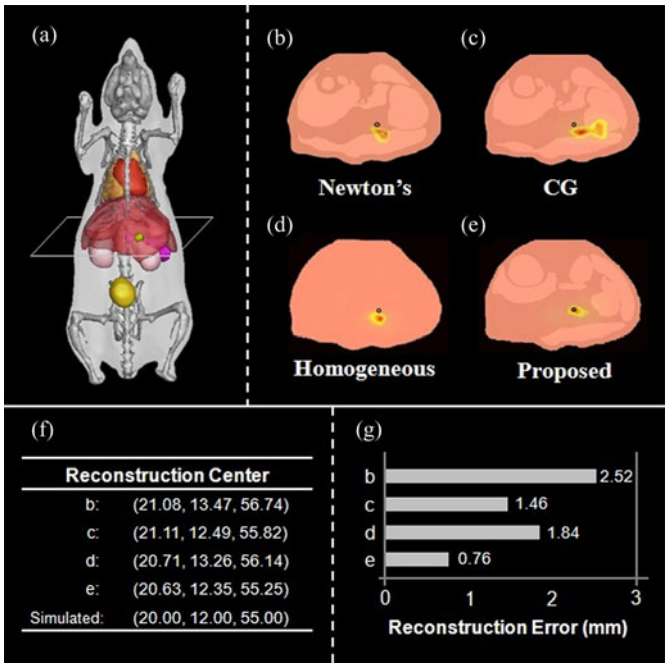

Fig. 6. Reconstruction results for the one-source case when $\lambda = 10^{-3}$: (a) 3-D view; (b)–(e) cross-sectional views, where the circle represents the location of the simulated bioluminescent source; (f), (g) numerical analysis for the reconstruction centers and errors in (b)–(e).

Newton method (Newton's) and the other was the CG [34]. The reconstruction results in cross-sectional views using Newton's and CG are given in Fig. 6(b) and (c), respectively. Besides, the corresponding numerical results are demonstrated in Fig. 6(f) and (g). The reconstruction error by Newton's was 2.52 mm, which was three times larger than that by the proposed method, while CG guaranteed a relatively smaller error of 1.46 mm. However, with the help of the anatomical structure shown in Fig. 6(c), it can be observed that artifacts appeared in the liver region by CG, which should not exist in precise reconstruction.

2) Robustness: To further evaluate the reconstruction performance, robustness testing was conducted for the proposed iterative reweighted l_2-norm optimization. Usually, the tomographic imaging quality is sensitive to the selection of the regularization parameter λ. Hence, λ with different orders of magnitude ranging from 10^{-1} to 10^{-20} were tested. The reconstruction results in cross-sectional views are partly demonstrated in Fig. 7(a)–(h). Although artifacts occurred when $\lambda = 10^{-1}$, for most cases, the reconstruction centers were still in good agreement with the simulated bioluminescent source center.

Furthermore, the corresponding numerical results are displayed in Fig. 7(i). According to the line graph, the reconstruction error undesirably reached its highest peak at 1.53 mm when $\lambda = 10^{-1}$, while it fell down to the lowest point when $\lambda = 10^{-3}$, followed by a slight change with a variation in λ. Particularly, the reconstruction error started to remain steady at 1.32 mm since $\lambda = 10^{-6}$. As can be concluded from the above results, the reconstruction results were satisfying and hardly affected by the different regularization parameters except when $\lambda > 10^{-3}$.

3) Efficiency: To examine the computational efficiency, Newton's and CG have been applied once again to reconstruct

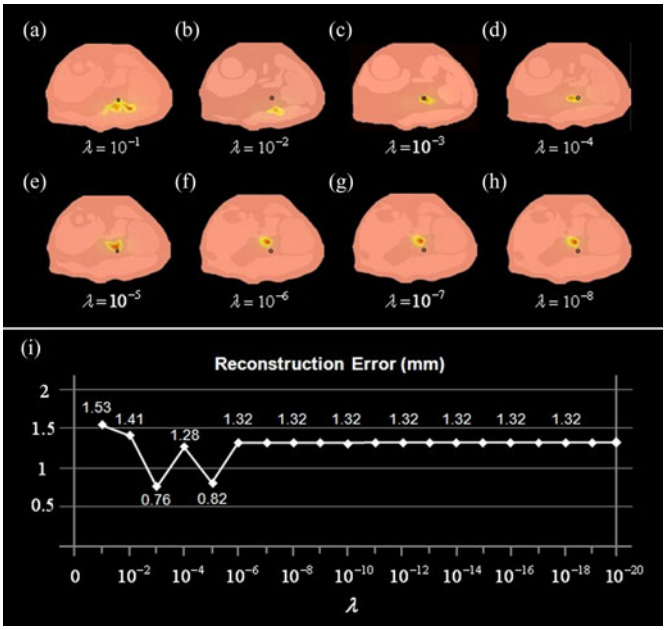

Fig. 7. Reconstruction results with different regularization parameters: (a)–(h) cross-sectional views when $\lambda = 10^{-1}, 10^{-2}, 10^{-3}, 10^{-4}, 10^{-5}, 10^{-6}, 10^{-7}, 10^{-8}$ respectively, where the circle represents the location of the simulated bioluminescent source; (g) numerical analysis for the reconstruction errors when $\lambda = 10^{-n}$, where n is an integer ranging from 1 to 20.

TABLE II
RECONSTRUCTION TIME OF NEWTON'S, CG, AND THE PROPOSED METHOD

Grid Size	Newton's	CG	Proposed
3397×18344	4605.48s	132.43s	9.28s
4529×21286	6925.12s	297.73s	10.74s

the same datasets in contrast to the proposed method. The reconstruction time of the three different methods has been compared in Table II, where the computations were based on two 3-D grids. For the grid of 3397 nodes and 18 344 tetrahedral elements, Newton's required more than 1 h to implement the reconstruction, while CG considerably enhanced the efficiency up to 132.43 s. Although CG can ensure good results within several minutes, it would become hardly tolerable to wait as the dataset size increases. Consequently, the proposed iterative reweighted optimization tended to be helpful and necessary. It took less than 10 s to complete the reconstruction process.

Similarly, for another grid of 4529 nodes and 21 286 tetrahedral elements listed in Table II, the proposed method was still much more efficient than the other two classical algorithms despite increasing grid size. The main reason leading to the substantial difference among the three methods is that the proposed method has employed an iterative shrinkage operator, which avoids the time-consuming computation of the matrix inversion. Besides, CG is more time saving than Newton's on account of not having to calculate the Hessian matrix, while Newton's has to calculate the matrix of second-order partial derivatives and its inversion.

4) Practical Application: To validate the feasibility of the proposed approach in a practical application, an *in vivo* mouse experiment has been conducted and its reconstruction results are

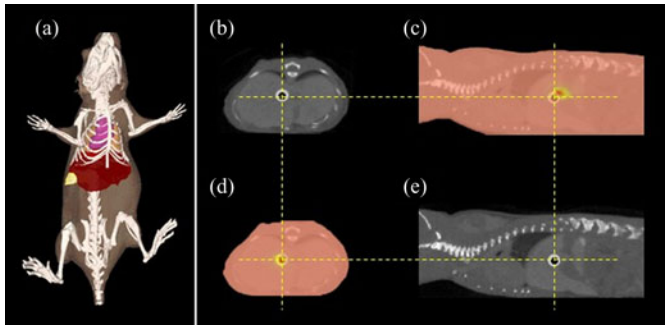

Fig. 8. Results for *in vivo* mouse studies: (a) 3-D view of the heterogeneous mouse model; (b), (e) transverse view and sagittal view of the CT slices, where the home-made luminescent bead can be observed approximately in the center; (c), (d) 2-D views of the reconstruction results, whose slice selections are the same as (b) and (e), respectively.

demonstrated in Fig. 8. In this experiment, a hairless mouse with a luminescent bead implanted in the liver region was utilized. The bead was filled with luminescent liquid which emitted a red luminescent light. After imaging, the micro-CT volume and bioluminescent images were acquired by the optical/micro-CT system. In order to build the heterogeneous mouse model, the micro-CT volume was segmented into several parts, which consisted of the skeleton, body outline, lungs, heart, liver, and stomach as displayed in Fig. 8(a). The corresponding optical properties were assigned to different organs and tissues according to Table I. Then, the 2-D bioluminescent images were mapped onto the 3-D micro-CT volume, so we could obtain the photon distribution of the bioluminescent signals on the mouse surface, which was indispensable for reconstruction.

As shown in Fig. 8(b) and (e), the location of the internal luminescent bead could be determined by the CT scan because the bead was wrapped in a plastic material. It examined the reconstruction accuracy of the bioluminescence tomography results in Fig. 8(c) and (d). For reconstruction, the grid contained 4529 nodes and 21 286 tetrahedral elements, while the regularization parameter λ was selected as 10^{-3} due to the experience in previous robustness testing. As a result, the reconstruction time was 10.74 s and the reconstruction error was 1.16 mm. Although the proposed method for the *in vivo* studies did not perform as well as that for the simulation studies, the reconstruction accuracy and efficiency were still acceptable.

C. Reconstruction Results: Multisource Cases

It has recently caught the attention of researchers to focus on multisource cases due to the actual demands for reconstructing more than one region of interest inside an experimental mouse, which therefore requires a reconstruction method capable of recovering more than one internal bioluminescent source. However, the method performs stably in a single source case, but it sometimes does not work in multisource cases because of the low optical image resolution as well as the low grid density employed to generate the photon diffusion model using finite element formulation. In this section, double/triple/quadruple source cases were designed to test how the proposed method behaved under different circumstances.

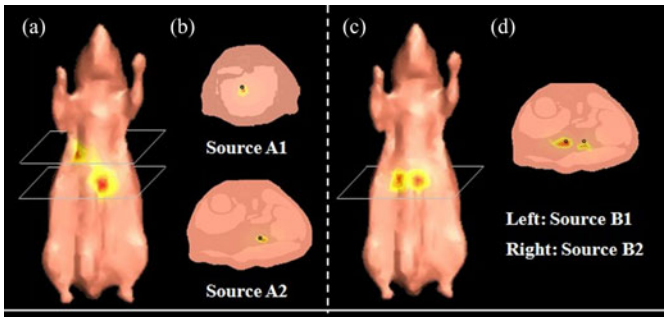

(e)

	Simulated Center	Reconstruction Center	Reconstruction Error (mm)
Source A1	(15.00, 10.00, 46.06)	(15.35, 10.52, 46.75)	1.08
Source A2	(20.00, 12.00, 55.00)	(20.44, 12.39, 55.28)	0.65
Source B1	(15.00, 12.00, 55.00)	(15.34, 12.59, 55.29)	0.74
Source B2	(20.00, 12.00, 55.00)	(20.11, 13.04, 55.48)	1.09

Fig. 9. Results for the double source case: (a) the heterogeneous mouse model with photon distribution on the surface, where the distance between two internal bioluminescent sources was 10 mm; (b) cross-sectional views of the reconstruction results when the distance was 10 mm; (c) surface photon distribution, where the distance between two internal bioluminescent sources was 5 mm; (d) cross-sectional view of the reconstruction results when the distance was 5 mm; (e) numerical analysis for the results in (b), (d).

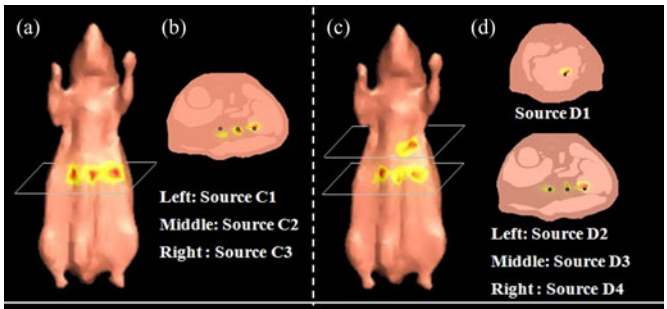

(e)

	Simulated Center	Reconstruction Center	Reconstruction Error (mm)
Source C1	(15.00, 12.00, 55.00)	(15.80, 12.92, 55.14)	1.23
Source C2	(20.00, 12.00, 55.00)	(20.58, 12.24, 55.70)	0.94
Source C3	(25.00, 12.00, 55.00)	(24.70, 11.93, 55.75)	0.81
Source D1	(20.00, 12.00, 45.00)	(20.56, 11.53, 45.85)	1.12
Source D2	(15.00, 12.00, 55.00)	(15.31, 11.68, 54.84)	0.47
Source D3	(20.00, 12.00, 55.00)	(20.73, 11.49, 55.42)	0.98
Source D4	(25.00, 12.00, 55.00)	(24.23, 11.70, 55.05)	0.83

Fig. 10. Results for triple and quadruple source cases: (a) surface photon distribution for the triple source case, where the shortest distance between two internal bioluminescent sources was 5 mm; (b) cross-sectional view of the reconstruction results for the triple source case; (c) surface photon distribution for the quadruple source case, where the shortest distance between the two internal bioluminescent sources was 5 mm; (d) cross-sectional views of the reconstruction results for the quadruple source case; (e) numerical analysis for the reconstruction results in (b), (d).

In the double-source cases, two experiments were carried out, where the distances between the two internal bioluminescent sources were 10 and 5 mm, respectively. As demonstrated in Fig. 9,the reconstruction errors were 1.08 and 0.65 mm when the two sources were 10 mm apart from each other, which was slightly better than that of the two being 5 mm apart. In the triple and quadruple source cases, the shortest distance between any two sources was 5 mm. As presented in Fig. 10, the reconstruction errors did not show a big difference from those of the double-source cases, but Sources D3 and D4 partly overlapped as shown in Fig. 10(d). It is necessary to note that: (i) the regularization parameter λ was selected as 10^{-3} during the reconstruction in all of the aforementioned cases (ii) the results were no longer satisfactory when the distance between the two sources was less than 5 mm.

IV. Conclusion

In this paper, we proposed an efficient algorithm using iterative reweighted l_2-norm optimization while taking structural information as priors to localize the internal bioluminescent signals. The structure priors have been applied to establish a heterogeneous mouse model by extracting the major organs and tissues of the mouse, thus generating a more precise photon diffusion model for the following reconstruction. To analyze the performance of the proposed method, both numerical simulation studies and *in vivo* mouse studies have been conducted.

The experimental results indicated that the iterative reweighted l_2-norm optimization is capable of guaranteeing accurate reconstruction for bioluminescence tomography. It maintains reliable reconstruction results with the changes in the regularization parameter λ, where the results are always satisfactory when $\lambda \leq 10^{-3}$. Regarding the same datasets, the proposed iterative reweighted approach computes faster than the two classical algorithms especially for the common high-dimensional problems in image processing. Besides, the reconstruction results of the *in vivo* experiment validated its feasibility in a practical application. The comparative analyses in one of the numerical simulation studies showed that the reconstruction based on the heterogeneous mouse model was about twice as precise as the one based on the homogeneous model. Last but not least, multisource cases have also been considered and the proposed method could provide acceptable results when the distance between two sources was not less than 5 mm.

Future work will concentrate on the study of the proposed method for more practical applications, e.g., to conduct *in vivo* experiments based on mice afflicted with tumors to determine if it is able to reconstruct the much weaker tumor signal. It is believed that bioluminescence tomography will provide more potential for earlier detection and characterization of the disease and evaluation of the treatment with rapid development of the 3-D reconstruction algorithms.

References

[1] V. Ntziachristos, "Going deeper than microscopy: The optical imaging frontier in biology," *Nat. Methods*, vol. 7, no. 8, pp. 603–614, 2010.

[2] F. G. Blankenberg and H. W. Strauss, "Recent advances in the molecular imaging of programmed cell death—Part II: Non-probe-based MRI, ultrasound, and optical clinical imaging techniques," *J. Nucl. Med.*, vol. 54, no. 1, pp. 1–4, 2013.

[3] S. Keereweer, J. D. F. Kerrebijn, P. B. A. A. van Driel, B. W. Xie, E. L. Kaijzel, T. J. A. Snoeks, I. Que, M. Hutteman, J. R. van der Vorst, J. S. D. Mieog, A. L. Vahrmeijer, C. J. H. van de Velde, R. J. B. de Jong, and C. W. G. M. Lowik, "Optical image-guided surgery—Where do we stand?" *Mol. Imaging Biol.*, vol. 13, no. 2, pp. 199–207, 2011.

[4] T. F. Massoud and S. S. Gambhir, "Molecular imaging in living subjects: Seeing fundamental biological processes in a new light," *Gene Develop.*, vol. 17, no. 5, pp. 545–580, 2003.

[5] C. H. Qin, S. P. Zhu, and J. Tian, "New optical molecular imaging systems," *Current Pharm. Biotechnol.*, vol. 11, no. 6, pp. 620–627, 2010.
[6] O. Leppanen, M. Ekstrand, and J. H. Braesen, "Bioluminescence imaging of energy depletion in vascular pathology: Patent ductus arteriosus and atherosclerosis," *J. Biophoton.*, vol. 5, no. 4, pp. 336–344, 2012.
[7] A. Rehemtulla, L. D. Stegman, S. J. Cardozo, S. Gupta, D. E. Hall, C. H. Contag, and B. D. Ross, "Rapid and quantitative assessment of cancer treatment response using in vivo bioluminescence imaging," *Neoplasia*, vol. 2, no. 6, pp. 491–495, 2000.
[8] Z. Paroo, R. A. Bollinger, D. A. Braasch, E. Richer, D. R. Corey, P. P. Antich, and R. P. Mason, "Validating bioluminescence imaging as a high-throughput, quantitative modality for assessing tumor burden," *Mol. Imaging*, vol. 3, no. 2, pp. 117–124, 2004.
[9] J. T. Au, L. Gonzalez, C. H. Chen, I. Serganova, and Y. Fong, "Bioluminescence imaging serves as a dynamic marker for guiding and assessing thermal treatment of cancer in a preclinical model," *Ann. Surg. Oncol.*, vol. 19, no. 9, pp. 3116–3122, 2012.
[10] X. W. Bai, Y. S. Yan, M. Coleman, G. Wu, B. Rabinovich, M. Seidensticker, and E. Alt, "Tracking long-term survival of intramyocardially delivered human adipose tissue-derived stem cells using bioluminescence imaging," *Mol. Imaging Biol.*, vol. 13, no. 4, pp. 633–645, 2011.
[11] J. E. Talmadge, "Bioluminescence in drug development for cancer Shedding light on therapeutic efficacy," *Cancer Biol. Ther.*, vol. 11, no. 9, pp. 846–848, 2011.
[12] R. Weissleder and V. Ntziachristos, "Shedding light onto live molecular targets," *Nat. Med.*, vol. 9, no. 1, pp. 123–128, 2003.
[13] G. Wang, Y. Li, and M. Jiang, "Uniqueness theorems in bioluminescence tomography," *Med. Phys.*, vol. 31, no. 8, pp. 2289–2299, 2004.
[14] C. H. Qin, S. P. Zhu, J. C. Feng, J. H. Zhong, X. B. Ma, P. Wu, and J. Tian, "Comparison of permissible source region and multispectral data using efficient bioluminescence tomography method," *J. Biophoton.*, vol. 4, no. 11–12, pp. 824–839, 2011.
[15] H. Zhao, T. C. Doyle, O. Coquoz, F. Kalish, B. W. Rice, and C. H. Contag, "Emission spectra of bioluminescent reporters and interaction with mammalian tissue determine the sensitivity of detection *in vivo*," *J. Biomed. Opt.*, vol. 10, no. 4, p. 041210, 2005.
[16] W. Guo, K. B. Jia, D. Han, Q. Zhang, X. Y. Liu, J. C. Feng, C. H. Qin, X. B. Ma, and J. Tian, "Efficient sparse reconstruction algorithm for bioluminescence tomography based on duality and variable splitting," *Appl. Opt.*, vol. 51, no. 23, pp. 5676–5685, 2012.
[17] A. Sangtae, J. C. Abhijit, D. Felix, A. B. Charles, and M. L. Richard, "Fast iterative image reconstruction methods for fully 3D multispectral bioluminescence tomography," *Phys. Med. Biol.*, vol. 53, no. 14, pp. 3921–3942, 2008.
[18] Y. J. Lv, X. Q. Zhang, A. Douraghy, D. Stout, J. Tian, T. F. Chan, and A. F. Chatziioannou, "Source reconstruction for spectrally-resolved bioluminescence tomography with sparse *a priori* information," *Opt. Exp.*, vol. 17, no. 10, pp. 8062–8080, 2009.
[19] A. Cong, W. Cong, Y. Lu, P. Santago, A. Chatziioannou, and G. Wang, "Differential evolution approach for regularized bioluminescence tomography," *IEEE Trans. Biomed. Eng.*, vol. 57, no. 9, pp. 2229–2238, Sep. 2010.
[20] J. Liu, D. Chen, X. Li, X. Ma, H. Chen, W. Fan, F. Wang, X. Qu, J. Liang, F. Cao, and J. Tian, "*In vivo* quantitative reconstruction studies of bioluminescence tomography: Effects of peak-wavelength shift and model deviation," *IEEE Trans. Biomed. Eng.*, vol. 57, no. 10, pp. 2579–2582, Oct. 2010.
[21] R. Noumeir, G. E. Mailloux, H. Mallouche, and R. Lemieux, "Comparison between Ml-Em and modified newton algorithms for SPECT image-reconstruction," in *Proc. Physiological Imaging, Spectroscopy, and Early-Detection Diagnostic Methods*, Los Angeles, CA, USA, 1993, vol. 1887, pp. 226–233.
[22] T. Tarvainen, M. Vauhkonen, and S. R. Arridge, "Gauss–Newton reconstruction method for optical tomography using the finite element solution of the radiative transfer equation," *J. Quant. Spectrosc. Radiat. Transf.*, vol. 109, no. 17–18, pp. 2767–2778, 2008.
[23] W. W. Zhu, Y. Wang, Y. Q. Yao, J. H. Chang, H. L. Graber, and R. L. Barbour, "Iterative total least-squares image reconstruction algorithm for optical tomography by the conjugate gradient method," *J. Opt. Soc. Amer. A*, vol. 14, no. 4, pp. 799–807, 1997.
[24] C. Byrne, "Block-iterative interior point optimization methods for image reconstruction from limited data," *Inverse Probl.*, vol. 16, no. 5, pp. 1405–1419, 2000.
[25] J. C. Ye, K. J. Webb, R. P. Millane, and T. J. Downa, "Modified distorted Born iterative method with an approximate Frechet derivative for optical diffusion tomography," *J. Opt. Soc. Amer. A*, vol. 16, no. 7, pp. 1814–1826, 1999.
[26] R. Roy and E. M. Sevick-Muraca, "Truncated Newton's optimization scheme for absorption and fluorescence optical tomography: Part II reconstruction from synthetic measurements," *Opt. Exp.*, vol. 4, no. 10, pp. 372–382, 1999.
[27] K. D. Paulsen and H. B. Jiang, "Enhanced frequency-domain optical image reconstruction in tissues through total-variation minimization," *Appl. Opt.*, vol. 35, no. 19, pp. 3447–3458, 1996.
[28] S. P. Zhu, J. Tian, G. R. Yan, C. H. Qin, and J. C. Feng, "Cone beam micro-CT system for small animal imaging and performance evaluation," *Int. J. Biomed. Imaging*, vol. 2009, no. 2009, p. 960573, 2009.
[29] G. R. Yan, J. Tian, S. P. Zhu, Y. K. Dai, and C. H. Qin, "Fast cone-beam CT image reconstruction using GPU hardware," *J. X-Ray Sci. Technol.*, vol. 16, no. 4, pp. 225–234, 2008.
[30] W. X. Cong and G. Wang, "Boundary integral method for bioluminescence tomography," *J. Biomed. Opt.*, vol. 11, no. 2, p. 020503, 2006.
[31] C. J. Miosso, R. von Borries, M. Argaez, L. Velazquez, C. Quintero, and C. M. Potes, "Compressive sensing reconstruction with prior information by iteratively reweighted least-squares," *IEEE Trans. Signal Process.*, vol. 57, no. 6, pp. 2424–2431, Jun. 2009.
[32] I. F. Gorodnitsky and B. D. Rao, "Sparse signal reconstruction from limited data using FOCUSS: A reweighted norm minimization algorithm," *IEEE Trans. Signal Process.*, vol. 45, no. 3, pp. 600–616, 1977.
[33] O. Scherzer, H. W. Engl, and K. Kunisch, "Optimal a posteriori parameter choice for Tikhonov regularization for solving nonlinear ill-posed problems," *SIAM J. Numer. Anal.*, vol. 30, no. 6, pp. 1796–1838, 1993.
[34] J. F. Bonnans, J. C. Gilbert, C. Lemaréchal, and C. A. Sagastizábal, *Numerical Optimization*. Berlin, Germany: Springer, 2006, pp. 51–76.

Authors' photographs and biographies not available at the time of publication.